

---

# PHYSICS CAPTURED BY DATA-BASED METHODS IN EL NIÑO PREDICTION

---

**G.Lancia, C.Spitoni**

Department of Mathematics  
Utrecht University, Netherlands  
g.lancia@uu.nl, c.spitoni@uu.nl

**I. J. Goede, H. Dijkstra**

Institute for Marine and Atmospheric research Utrecht, Department of Physics  
Utrecht University, Netherlands  
i.j.goede@students.uu.nl, h.a.dijkstra@uu.nl

## ABSTRACT

On average once every four years, the Tropical Pacific warms considerably during events called El Niño, leading to weather disruptions over many regions on Earth. Recent machine-learning approaches to El Niño prediction, in particular Convolutional Neural Networks (CNNs), have shown a surprisingly high skill at relatively long lead times. In an attempt to understand this high skill, we here use data from distorted physics simulations with an intermediate complexity El Niño model to determine what aspects of El Niño physics are represented in a specific CNN-based classification method. We find that the CNN can adequately correct for distortions in the ocean adjustment processes, but that the machine-learning method has far more trouble to deal with distortions in upwelling feedback strength.

**Keywords** Data-driven approaches to advance climate sciences · Artificial Intelligence · Atmospheric and oceanic physics

## 1 Introduction

Interannual climate variability is strongly dominated by the El Niño-Southern Oscillation (ENSO) in the Tropical Pacific. During an El Niño, the positive phase of ENSO, sea surface temperatures in the eastern Pacific increase by a few degrees with respect to seasonally averaged values; the oscillation phase opposite to El Niño is La Niña, with a colder eastern Pacific. A much used measure of the state of ENSO is the NINO3.4 index, which is the area-averaged Sea Surface Temperature (SST) anomaly (i.e. deviation with respect to the mean seasonal cycle) over the region  $170^{\circ}\text{W}-120^{\circ}\text{W} \times 5^{\circ}\text{S}-5^{\circ}\text{N}$ . El Niño events typically peak in December, occur every two to seven years, and their strength varies irregularly on decadal time scales. The spatial pattern of ENSO variability is often determined from principal component analysis [Preisendorfer, 1988, ], detecting patterns of maximal variance. At least two different types of El Niño events exist [Zhang et al., 2019, ], with largest temperature anomalies either in the eastern Pacific (Eastern Pacific or EP El Niño's) or near the dateline (Central Pacific or CP El Niño's).

As ENSO has distinct influences on the climate around the globe through well-known teleconnections, skillfull predictions of up to a one year lead time are desired to be able to mitigate the effects [Balmaseda et al., 1995, ]. For ENSO predictions, often the Oceanic Niño Index (ONI) is used, which is defined as the three-month running mean of the NINO3.4 index. Both statistical models (those capturing behaviour of past events) and dynamical models (i.e. those based on the underlying physical conservation laws) are used for El Niño prediction [Latif et al., 1998, Chen and Cane, 2008, Barnston et al., 2012b, Saha et al., 2014, Timmermann et al., 2018, Tang et al., 2018, ]. El Niño events are difficult to predict as they have an irregular occurrence, and each time have a slightly different development [McPhaden et al., 2015, Timmermann et al., 2018, ]. Many ENSO prediction evaluation studies

[Barnston et al., 2012a, L’Heureux et al., 2017, ] have shown that dynamical models do better than statistical models and when initialized before the boreal spring, most models perform much worse than when initialized in summer. The latter notion has been indicated by the spring predictability barrier problem [McPhaden, 2003, ].

ENSO theory [Neelin et al., 1998, ] provides a framework to understand the existence of such predictability barriers. The ENSO phenomenon is thought to be an internal mode of the coupled equatorial ocean-atmosphere system which can be self-sustained or excited by small-scale processes, often considered as noise [Fedorov et al., 2003, ]. Bjerknes’ feedbacks are central in the amplification of SST anomalies, whereas equatorial ocean wave processes provide a delayed negative feedback, and are responsible for the time scale of ENSO. The interactions of the internal mode and the external seasonal forcing can lead to chaotic behavior through nonlinear resonances [Tziperman et al., 1994, Jin et al., 1994, ]. On the other hand, the dynamical behavior can be strongly influenced by noise, in particular westerly-wind bursts [Lian et al., 2014, ]. During boreal spring and summer the Pacific climate system is most susceptible to perturbations leading to predictability barriers [Latif and Barnett, 1994, ]. The growth of perturbations from a certain initial state has been investigated in detail from a much used intermediate-complexity model, the Zebiak-Cane model [Zebiak and Cane, 1987, ]. Applying the methodology of optimal modes [Mu et al., 2007, Duan et al., 2009, Yu et al., 2012, ], it was indeed shown that spring is the most sensitive season for EP El Niños and likewise summer for CP El Niños [Tian and Duan, 2015, Hou et al., 2019, ].

Deep-learning methods (DLMs) are powerful statistical models which have now been used in a wide range of applications such as speech recognition and image reconstruction [Goodfellow et al., 2016, ]. These methods include feed-forward Artificial Neural Networks (ANNs), Recurrent Neural Networks (RNNs), Reservoir Computers (RCs), and Convolutional Neural Networks (CNNs); over quite some time now, DLMs have been applied to El Niño prediction [Dijkstra et al., 2019]. The current work is motivated by the high El Niño prediction skill of two types of DLMs. First, in [Ham et al., 2019a, ] CNNs were trained on model data from the Climate Model Intercomparison Project, phase 5 (CMIP5) using transfer learning and subsequently trained on reanalysis data. The CNN-based scheme shows a better forecasting skill than most dynamical models and this forecast skill remains high up to lead times of about 17 months. It is also able to successfully predict the type of El Niño (CP- or EP) patterns which develop. Second, in [Petersik and Dijkstra, 2020, ], Deep Ensemble Methods [Lakshminarayanan et al., 2017, ], in particular Gaussian Density Neural Networks (GDNNs) and Quantile Regression Neural Networks (QRNNs), were used in ENSO prediction. These methods also give a skillful model for the long-lead time prediction of the ONI (and its uncertainty) using a relatively small predictor set.

At the moment, there is an enormous effort to understand the performance of DLMs generally referred to as explainable AI [Arrieta et al., 2020, ]. The research described above shows that DLMs are a very promising tool in ENSO prediction that can provide useful skill of El Niño forecasts beyond the predictability barriers. The intriguing question is now what the DLMs capture of the ENSO physics contained in the data. Addressing this question is precisely the focus of this paper. We will approach this issue using the Zebiak-Cane model, which is also routinely used for ENSO prediction. The novel aspect of this work is that we use so-called distorted physics experiments where different physical processes (such as equatorial wave dynamics and ocean-atmosphere feedbacks) are perturbed. Using saliency analyses, determining which input variables contribute most to the prediction skill, we then aim to determine what part of the ENSO dynamics is represented by the DLM.

## 2 Models and Methods

### 2.1 ENSO model

The Zebiak-Cane (ZC) model [Zebiak and Cane, 1987, ] represents the coupled ocean-atmosphere system on an equatorial  $\beta$ -plane in the equatorial Pacific. In this model, a shallow-water ocean component is coupled to a steady shallow-water Gill [Gill, 1980, ] atmosphere component. The atmosphere is driven by heat fluxes from the ocean, depending linearly on the anomaly of the sea surface temperature  $T$  with respect to a radiative equilibrium temperature  $T_0$ . We use the numerically implicit fully-coupled version of this model, developed in [van der Vaart et al., 2000], and slightly extended in [Feng and Dijkstra, 2017]. In this version, the zonal wind stress  $\tau^x$  is written as

$$\begin{aligned}\tau^x &= \tau_{ext}^x + \tau_c^x, \\ \tau_{ext}^x &= -\tau_0 e^{-\frac{1}{2}\left(\frac{y}{L_a}\right)^2}.\end{aligned}\tag{1}$$

Here the external part  $\tau_{ext}^x$  represents a weak ( $\tau_0 \sim 0.01 Pa$ ) easterly wind stress due to the Hadley circulation,  $L_a$  is the atmospheric Rossby deformation radius and  $y$  is the meridional coordinate. The zonal wind stress  $\tau_c^x$  is proportional to the zonal wind from the atmospheric model which, in turn, depends on sea surface temperature.

As shown in [van der Vaart et al., 2000], the parameter measuring the strength of all ocean-atmosphere coupled feedbacks is the coupling strength  $\mu$ . When  $\mu < \mu_c$ , where  $\mu_c$  indicates a critical value, the Tropical Pacific climatology (a

stationary state of the model) is stable. However, if the coupling strength exceeds the critical value  $\mu_c$ , a supercritical Hopf bifurcation occurs and sustained oscillations occur with a period of approximately four years. A seasonal cycle is included in the model by varying  $\mu$  over time with a specific amplitude  $\Delta\mu$  and with an annual period.

Apart from the coupled ocean-atmosphere processes, ENSO is also affected by fast processes in the atmosphere, such as westerly wind bursts. These processes are considered as noise in the ZC model. The representation of atmospheric noise in the model is similar to that in [Feng and Dijkstra, 2017], where the westerly wind bursts are represented by one Empirical Orthogonal Function pattern (with the associated principle component fitted to an AR(1) process) in the zonal wind stress. The observation-based data set in [Feng and Dijkstra, 2017] contains weekly patterns of this wind-stress noise. In the ZC model, we randomly add one of such patterns at each time step (of a week) to the zonal wind stress. The effect of the noise on the model behavior depends on whether the model is in the super- or sub-critical regime (i.e whether  $\mu$  above or below  $\mu_c$ ). If  $\mu < \mu_c$ , the noise excites the ENSO mode, causing irregular oscillations. In the supercritical regime, the cycle of approximately four years is still present, but the noise causes an irregular amplitude of ENSO variability.

## 2.2 Distorted physics simulations

The advantage of the ZC model is that the behavior of the model can be connected to the physical processes in a very transparent way [Jin, 1997b, ]. For this model, we define a ‘truth’ by a reference simulation, using an external seasonal cycle, prescribed noise in the wind-stress and parameter settings such as in [Feng and Dijkstra, 2017]. Next, in subsequent distorted-physics simulations we change the representation of physical processes in the model by varying parameters. We will focus on the main processes setting the time scale and amplitude of ENSO.

An important memory component in the Tropical Pacific climate system is the ocean adjustment to changes in the atmospheric forcing. This is accomplished by equatorial wave dynamics and best described by a basin mode response, where the basin mode consists of a sum of one Kelvin and multiple Rossby waves. In the SST-mixed ocean dynamics mode framework behind ENSO variability [Neelin et al., 1998, ], the adjustment is crucial for the timing of El Niño events. It plays also a crucial role in the recharge/discharge oscillator view of ENSO [Jin, 1997a, ], where the equatorial heat content is varied, usually measured by the Warm Water Volume in observations. The temporal aspects of the adjustment can be controlled in the Zebiak-Cane model by putting a coefficient  $\delta$  before the time derivatives of the ocean momentum equations [Neelin, 1991, ]. In the extreme case where the time derivative is effectively zero ( $\delta = 0$ ), the so-called ‘fast-wave’ limit is reached.

Three of the most important positive Bjerknes’ feedbacks are the thermocline feedback, the zonal advection feedback and the upwelling (or Ekman) feedback [Dijkstra, 2005, ]. The relative magnitude of these feedbacks determines which spatial SST perturbation patterns are amplified. In addition, the feedbacks determine also the mean state and seasonal cycle of the tropical Pacific climate state [Dijkstra and Neelin, 1995, ]. Specific feedback strengths can be changed in the ZC model by varying the mean thermocline depth (thermocline feedback), the mean zonal temperature gradient (zonal advection feedback), or Ekman friction (upwelling feedback). We will concentrate on the latter feedback, affecting the amplitude of ENSO, and which can be changed in the ZC model by adjusting the parameter  $\delta_s$ .

## 2.3 CNN approach

Due to their versatility and peculiarity in solving binary and multi-labels classification tasks by capturing and recognizing the discerning patterns of the input data, CNNs (Convolutional Neural Networks) can represent a powerful method for making forecasting of ENSO events with lead times of up to one and a half years [Ham et al., 2019b, ] or for solving a binary classification problem in hybrid models with high complexity multi-resolution input data [Yan et al., 2020, ]. Unlike more sophisticated and popular ANNs like CNN-LSTM and ConvLSTM, the predictions provided by the CNN can be made explainable by means of saliency maps [Adebayo et al., 2018, Selvaraju et al., 2017, Zhou et al., 2016, Montavon et al., 2019, Mundhenk et al., 2019, ] that allow to outline the spatial locations of those signal patterns that mainly contribute to make the CNN give the classes of output. Therefore, CNNs represent the perfect choice for classifying the occurrence of ENSO events in ZC simulations and investigating in detail on which features contained in data can lead to highly accurate predictions. To leverage the basic feature of the CNN of encoding the sequentiality of the patterns contained in the input data, we feed the CNN with simulated time series obtained via Zebiak-Cane model. This synthetic data set describes the temporal evolution in the NINO3.4 region of some physical observables of interest as the thermocline depth, the sea surface temperature, the wind speed and the wind stress noise. The extraction of the instances from the ZC simulations therefore consists in slicing the synthetic time series along the time-domain, i.e. the set of time series is chunked in a sequence of overlapping time windows of 48 months and stride 1. As a result, each single instance is a tensor of rank 2 whose dimensions are the time-length (48 pixels, sampling frequency one month) and the number of time series features (the four physical observables of interest).

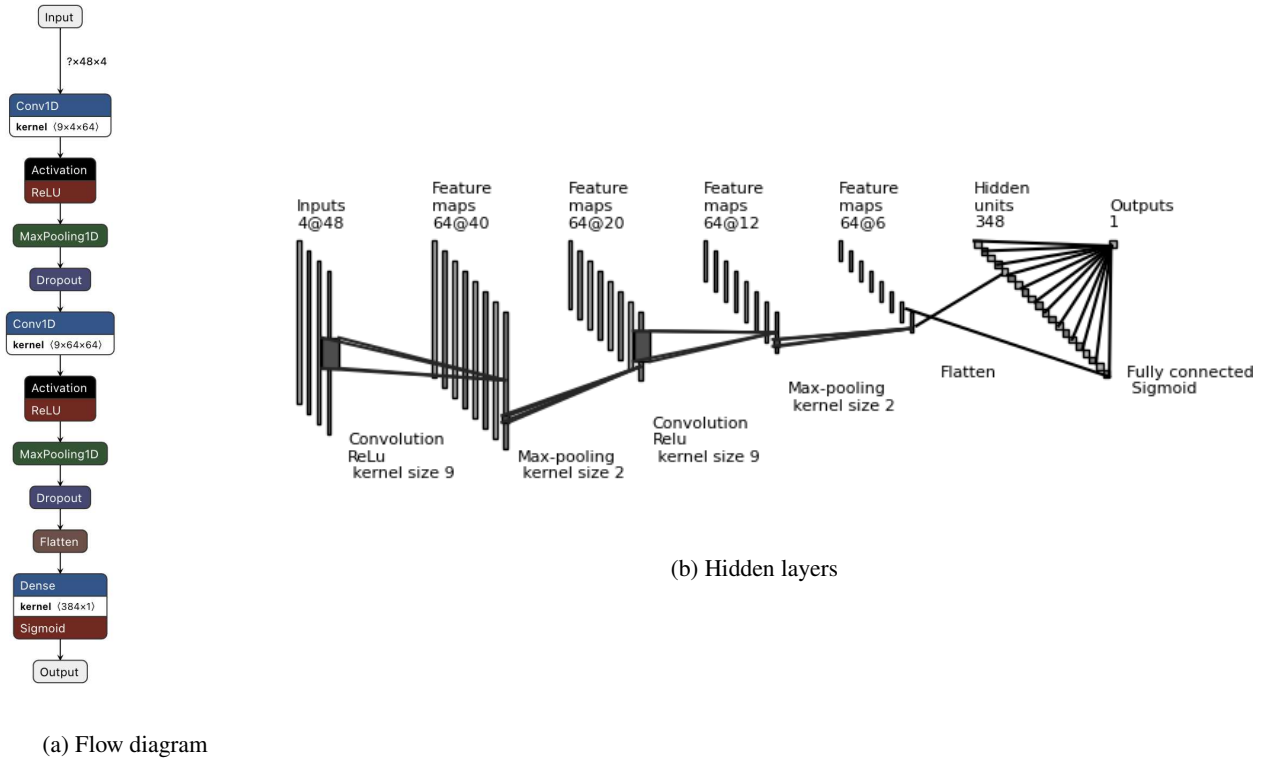


Figure 1: Schematic illustrations of the CNN model

The labeling of the instances is performed by equipping each instance with the corresponding ONI-index value, and so we label one ENSO event whenever the ONI-index value is greater than 0.5 (El Niño event) or lower than -0.5 (La Niña event). The inputs instances are then pre-processed via standardization (each feature has now zero-mean and unit variance) and divided into training set and test set; we validate the CNN model by means of the 5-fold cross-validation. Therefore we evaluate the AUC (Area Under the Curve) of the receiver operating characteristic curve on each fold; the mean value and the standard error mean will provide the degree of accuracy of the CNN model and its error respectively. The design of our CNN is quite standard and it is composed by the sequence of one convolutional layer (64 kernels, size 9) with a Rectified Linear Unit (ReLU) activation function, followed by a maxpooling Layer with pooling size 2 (Fig. 1). Dropout layers [Srivastava et al., 2014, ] with dropout rate 0.50 are also employed to reduce overfitting, but no stride is applied during the convolutions. After repeating two times this block of hidden layers the resulting feature map is flattened via a flatten layer; the final fully-connected layer with sigmoid activation function returns the output of the CNN. During the training phase the ADAM [Kingma and Ba, 2014, ] algorithm is used as optimizer for the Binary-Cross Entropy loss function; the batch size and learning rate are set equal to 128 and 0.005, respectively. SMOE scale method [Mundhenk et al., 2019, ] is a novel and robust measure statistics of the activation values of CNNs arising at different spatial locations (temporal locations in the domain of our instances). This statistics can be used to construct robust saliency maps that appears to be much more efficient and computationally faster than popular gradient methods. We therefore exploit the capability of SMOE scale method to detect those patterns and their spatial domains that mostly indicate the approaching or the occurring of the ENSO events. Thus, we proceed with the analysis of the profile of the saliency maps in order to evince possible analogies and differences between the patterns learnt during the training phase and the patterns contained in the test data set. In order to complete the analysis provided by the SMOE scale method, we even look at how the predictions can change when only a spectral sub-band of the input instances is propagated through the hidden layers.

With this approach we aim to investigate how oscillations occurring under a specific regime can really be a basic aspect of the prediction provided by the CNN. Therefore, we can progressively apply a digital Butterworth ([Butterworth et al., 1930], [Hamming, 1998]) filter of order 3 as either a bandpass filter or low-pass filter to smooth the input instance. The ensemble of bandpass filters are designed to cover the whole spectral domain of any input instance and be non-overlapping at the same time and thus we impose the cutoff frequencies of each filter to be in ratio 1:2. This means that, starting from the Nyquist frequency  $\nu_0$ , the first digital filter will have its frequency band in  $[\frac{\nu_0}{2}, \nu_0]$ , the second one in  $[\frac{\nu_0}{4}, \frac{\nu_0}{2}]$ , and so on. Again, when considering the low-pass digital filters we will choose

Table 1: Frequency bands and cut-off frequencies for the band-pass and low-pass digital filters, respectively

Frequency bands (Period in months)	Cut-off period (months)
[2, 4)	2
[4, 8)	4
[8, 16)	8
[16, 32)	16
[32, 48)	32

 Table 2: Parameter settings of the ZC model used to generate the data used in the distorted physics experiments with the parameter step size shown within brackets. Parameter ranges are chosen to cover roughly a 50% increase and decrease compared to reference value, step size is chosen to get around 10 points within this range. The parameters are from left to right: coupling strength  $\mu$ , wave speed parameter  $\delta$  and upwelling feedback parameter  $\delta_s$ . The value of  $\mu = 2.7$  is subcritical in the ZC model.

effect	$\mu$	$\delta$	$\delta_s$	$\delta_{sst}$
distorted wave speed	2.7	0.5-1.5 (0.1)	0.3	1.0
distorted wave speed	2.7	0.5-1.5 (0.1)	0.3	1.0
distorted upwelling	2.7	1.0	0.1-0.6 (0.05)	1.0
distorted upwelling	2.7	1.0	0.1-0.6 (0.05)	1.0
reference	2.7	1.0	0.3	1.0

the cut-off frequency according to a dyadic scale, i.e. the first filter will have cut-off frequency  $\nu_0$ , the second one  $\frac{\nu_0}{2}$ , the third one  $\frac{\nu_0}{4}$  and so on. The full list of bandwidths (in periods) and cutoff frequencies is reported in Table 1. Note that we will apply these digital filtering techniques by repeating the same 5-fold cross validation with metrics AUC, as we do in the model validation; the CNN architecture will not be altered during this step. Hence, by means of this approach we aim to reveal which time scale is dominant in those patterns that characterize the ENSO events (e.g. a slow oscillating trends against rapid oscillating deviations), i.e. we make an effort to understand how the periodicity of the time series features is an essential characteristic of data that the CNN captures for solving the classification task and how a distortion of it can give rise to a decrease in the CNN capability of classifying the El Niño and La Niña events.

### 3 Results

#### 3.1 Distorted physics

The model experiments broadly consist of two steps: first the ZC model is run for standard parameter values to produce reference case data. Then it is ran again but for a range of values around the standard parameter value (shown in Table 2) to get the distorted data. This ultimately results in three different kinds of datasets: reference case, distorted wave speed and distorted upwelling feedback. There are no simulations where more than one parameter is distorted at the same time. In the second step, the distorted datasets are used as training data for the DLMs whose performance is then determined by using the reference case as the test set. As a consistency check the DLMs are also trained on the reference case data and then tested on reference case data. This should produce the highest performance because the DLMs are tested on data they have already seen.

#### 3.2 Equatorial wave dynamics

Time series of the ONI for the different  $\delta$  values, as computed from the ZC model are shown in Fig. 2. Changing the  $\delta$  value causes the amplitude of the oscillation to become much smaller for  $\delta < 1$ , so much even that by definition only ENSO neutral conditions ( $-0.5 < ONI < 0.5$ ) are present. Increasing  $\delta$  above the reference value of 1.0 initially leads to an increase in the oscillation amplitude and it then decreases again for higher values of  $\delta$ . This is expected because the ENSO period depends on the speed of Rossby and Kelvin waves crossing the Pacific basin. In the study of the classification performance of the CNN, we take a prediction lead time of 9 months. The propagation of the  $\delta$ -distorted data through the CNN can lead to substantial changes when testing the accuracy of model on the reference data. By construction, the AUC score (Fig. 3) attains excellent results at  $\delta = 1.0$  (AUC 0.94) as the CNN is trained on the reference data. The AUC scores tend to remain relatively high (peak of AUC 0.91 at  $\delta = 0.8$ ) as the  $\delta$  parameter is slightly decreased from its reference value. Instead, as  $\delta$  is reduced up to value 0.5 we can observe a severe degradation of the accuracy with respect to the reference case; from  $\delta = 0.7$  the evaluation of the AUC metrics

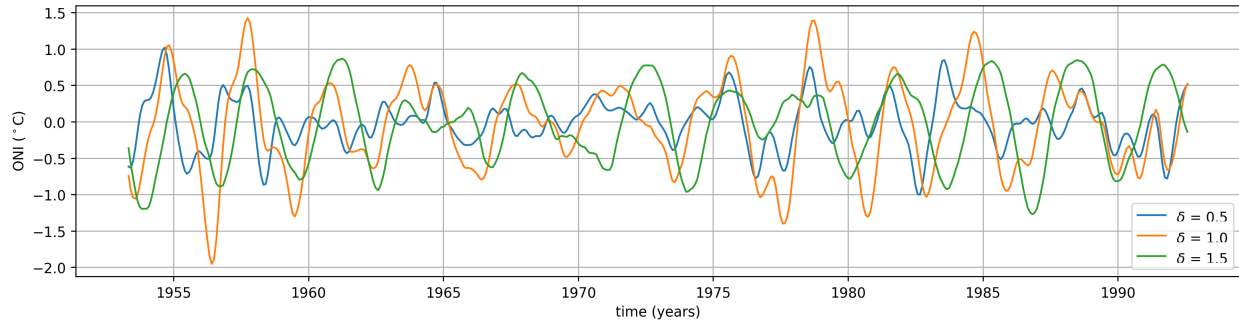


Figure 2: Several time series of ONI calculated from ZC model simulations using  $\delta$  parameter values of 0.5, 10 and 1.5, respectively.

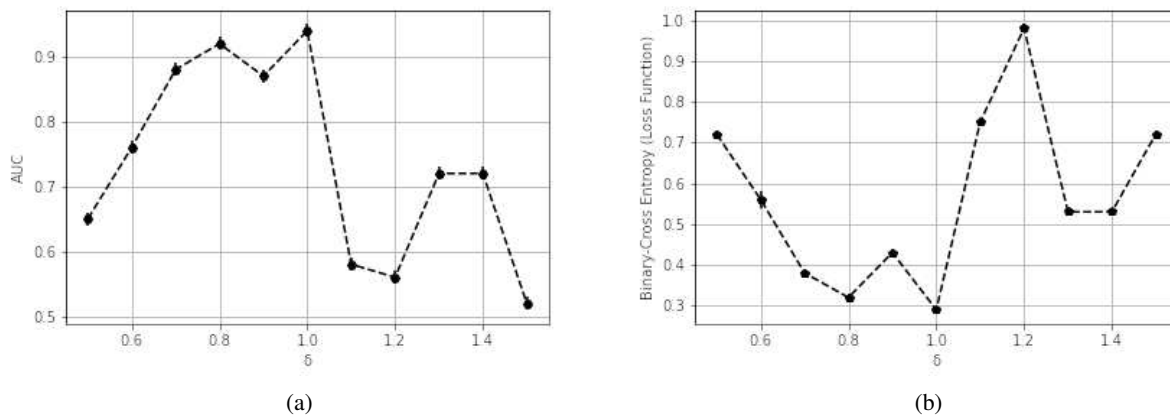


Figure 3: The AUC score (a) and the loss function (b) as a function of the equatorial wave speed  $\delta$ . Each point represents the mean AUC over 5 different folds; error bars are evaluated via standard error mean.

decreases monotonically (AUC 0.66 at  $\delta = 0.5$ ). At values  $\delta > 1.0$  we observe a total reduction of the AUC values. Specifically, models trained for  $\delta = 1.1$ , and  $\delta = 1.2$  show low AUCs as 0.58 and 0.56 but the lowest value (AUC value 0.51) is reached at  $\delta = 1.5$ . The evaluation of the loss function (when the reference data are propagated through the CNN models) confirms the scenario expressed above. Indeed, the global minimum value is achieved at  $\delta = 1.0$  and a relative minimum is also present at  $\delta = 0.8$ . When  $\delta$  is decreased or augmented towards the bound values  $\delta = 0.5$  and  $\delta = 1.5$  respectively, we can observe the loss function tends to reach higher values. In particular, an increase or decrease in the AUC along the  $\delta$  domain is followed by a decrease or an increase in the loss function.

The application of combined SMOE Scale to the mean instances (namely, the instances obtained by averaging all samples of the test data) can help identifying which patterns in the data are captured by the CNN to generate (accurate or degraded) ONI predictions. The reasons of analyzing the mean instance is that it represents the main patterns in the feature time series; the interpretation of the saliency maps of all instances would turn out to be really unpractical. The mean instances for both El Niño and La Niña events for all four features are shown in Fig. 4a-b. The saliency map of the  $\delta = 1$  reference case (green curve in Fig. 4c) shows two peaks with intensity 0.6 and 0.8 around month 18 and 35, respectively (note that the instances are 48 months long and that the lead time is 9 months). These two regions are the most salient along the whole instance domain for El Niño prediction and are associated with a doublet of peaks in the thermocline depth (Fig. 4a) and a doublet of troughs of both sea surface temperature (Fig. 4c) and wind speed (Fig. 4e). Therefore, this combination of patterns in the time series features represents the characteristic that mostly define the El Niño events.

Likewise, the saliency maps of the mean instance of the event class La Niña achieves values larger than 0.8 at similar temporal locations corresponding to peaks in the thermocline depth and some troughs in the sea surface temperature and wind speed. For the cases  $\delta = 0.5$  and  $\delta = 0.8$  (where waves are propagating faster than the reference case), the detection of peaks in the thermocline is associated to troughs in the sea surface temperature and vice versa; this combination of patterns can still lead to a relevant contribution to classify the ENSO events. For the event El Niño,

Physics captured by data-based methods in El Niño prediction

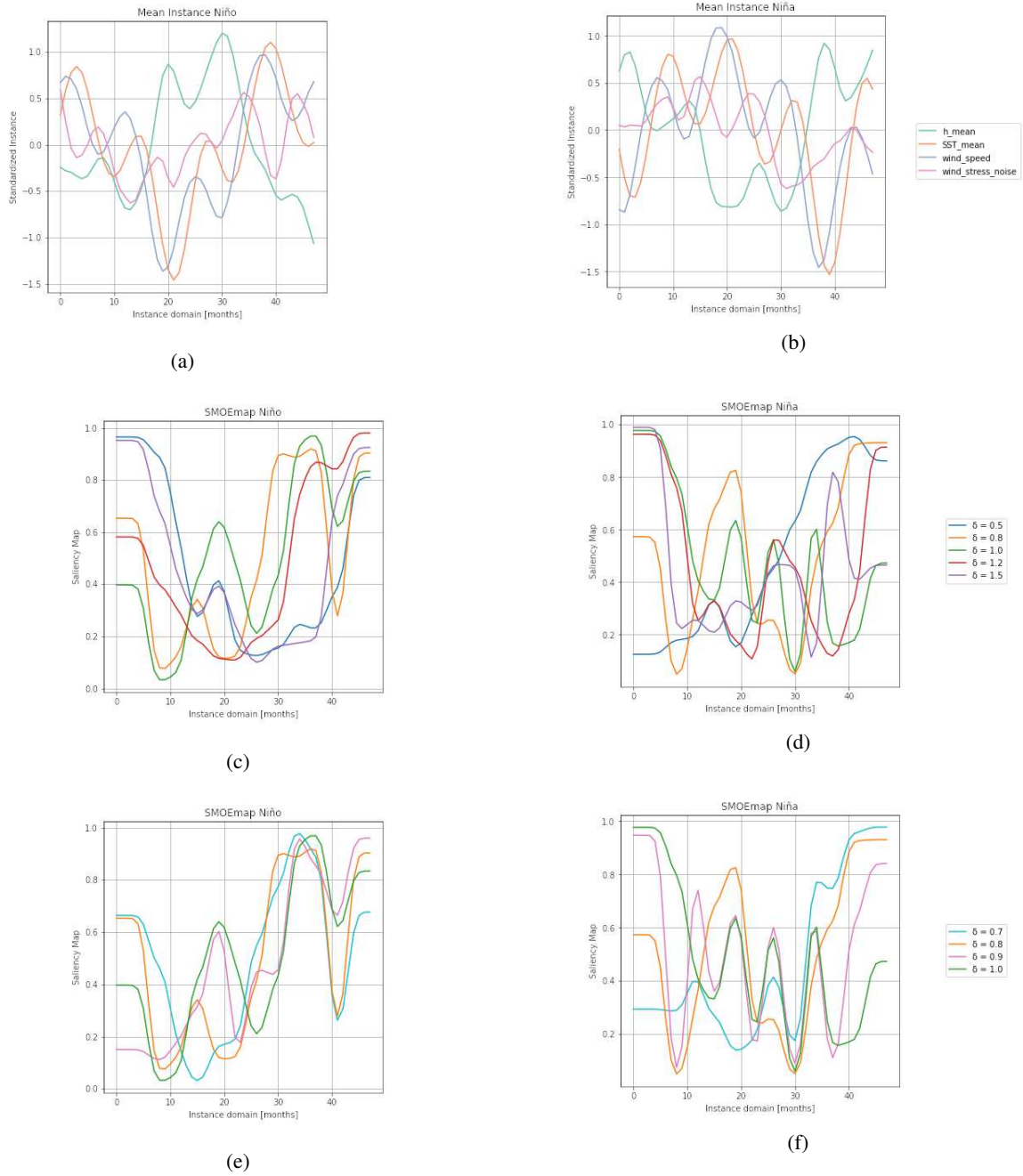


Figure 4: Representation of the mean instance of the test data (reference case; Figs. (a)-(b)) and its saliency maps (Figs. (c)-(f)) for the wave distorted case (variation of  $\delta$ ). For the event class El Niño the mean instance and its saliency maps are reported on the left column, while on the right column the results for the class La Niña are shown.

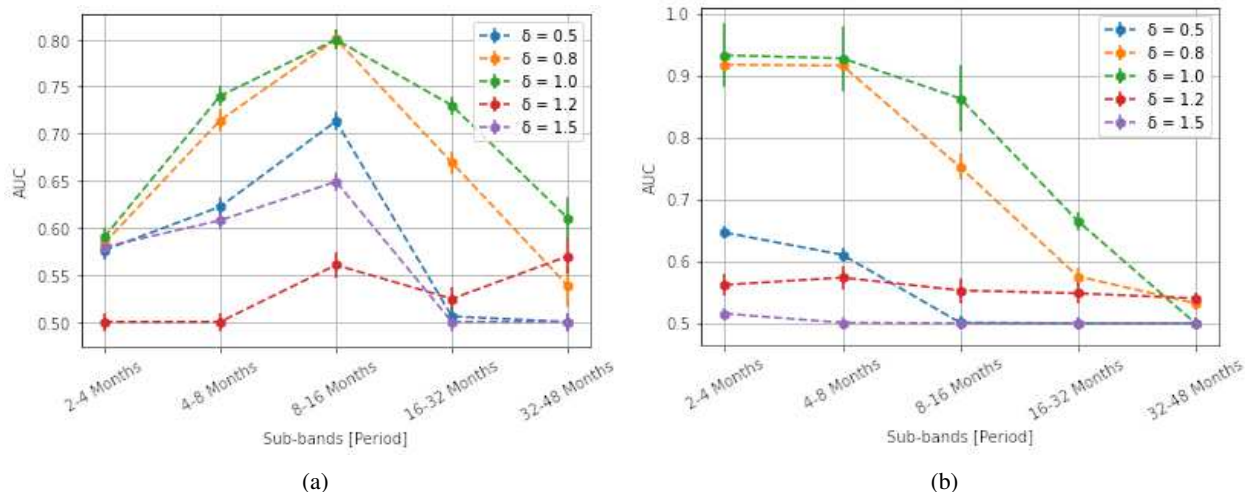


Figure 5: The AUC score for different values of  $\delta$  for the event El Niño as a function of (a) the band-pass frequency range and (b) the cut-off frequency, obtained by filtering the data by (a) band-pass Butterworth digital filter and (b) a low-pass Butterworth digital filter.

case  $\delta = 0.8$  shows a broad and flat peak with intensity larger than 0.8 in the saliency map around month 35 and the CNN is still able to capture patterns located nearby at the same months as for the reference case; case  $\delta = 0.5$  shows high intensities in the saliency map in the region 0-10 months. Here the thermocline depth shows a soft minimum value opposed to the high valued peak in the the sea surface temperature and wind speed. A deeper insight into the region  $\delta = 0.7 - 1.0$ , where the AUC attains the highest values, can reveal that the CNN models can capture the similar patterns likewise the case  $\delta = 0.8$  (Figs. 4e-f). Indeed, the saliency maps of both cases  $\delta = 0.7$  and  $\delta = 0.9$  reveal the presence of a large and broad peak with intensity larger than 0.8 at month 35; the case  $\delta = 0.9$  shows that the pattern recognition activity is much more similar to the model trained under the reference case, since its saliency map can point out some other details of interest, e.g. the peak with intensity 0.6 at month 18.

Similar results are obtained for the event La Niña. On the other hand, the results for the cases  $\delta = 1.2$  and  $\delta = 1.5$  (where waves are propagating slower) reveal that the maximum at 18 months disappears in the saliency map, but the main contributions can be found either around month 35 or at 0-10 months. For case  $\delta = 1.2$ , the event El Niño is characterized by the combination of a broad peak in both the sea surface temperature and the wind speed with a less important contribution (than in the reference case) in the thermocline depth located at months 32-48; for case  $\delta = 1.5$  we can observe a behaviour similar to case  $\delta = 0.5$  in the saliency map. Instead, the La Niña event for case  $\delta = 1.2$  is mainly characterized by the opposite feature, i.e. a broad peak in the thermocline depth and a trough in the sea surface temperature at located at months 0-10; likewise case  $\delta = 1.5$  is characterized by the same feature of  $\delta = 1.2$  but located at months 32-48. The application of a band-pass filter on all the sample instances of the test dataset (reference case data) reveals that the information retained in one specific frequency bands can partially retrieve the AUC scores obtained with the non-filtered data. The model trained under the reference case turns out to be very sensitive to the frequency bands corresponding to periods 8-16 months with AUC 0.80 (Fig. 5a). On the contrary, a complete degradation of AUC scores is attained at lower and higher frequency bands, e.g. in both intervals 16-32 months and 2-4 months we observe an AUC value of 0.58. Similar results can be found for all other cases taken under consideration, i.e. the band 8-16 months represent the most predictive one with a net degradation of AUC score as soon as slower frequency bands are considered. Note that case  $\delta = 0.8$  still show some analogies with the reference case; the frequency band 8-16 months is the most predictive with AUC score 0.80. Therefore, this result points out that the activation of the hidden layers showed with the analysis of the saliency map can be traced to the detection of oscillating trends with specific carrier frequencies within a low-medium band of frequencies. The presence of details on a shorter frequency scale (i.e. period 16-32 months), however, is still fundamental and needed to allow the CNN to make an accurate classification of the event El Niño. The smoothing of the sample instances with a low-pass filter (Fig. 5b) reveals the instances tend to substantially loose many of their discriminating patterns at cutoff frequencies corresponding to 8 or 16 months. For example, in the cases  $\delta = 0.8$  and  $\delta = 1.0$  we can observe a decrease of the predictive power with a degradation of 0.1 AUC at 8 months and 0.3 AUC at 16 months. Hence, medium-low frequency patterns (4-8 months) as those contained in the thermocline depth or in the wind-noise time series can play an important role in the detection of the events. Finally, to ensure the correct implementation of the combined SMOE Scale and to guarantee the validity of the results obtained, we used (and adapted to our analysis) the metrics ROAR



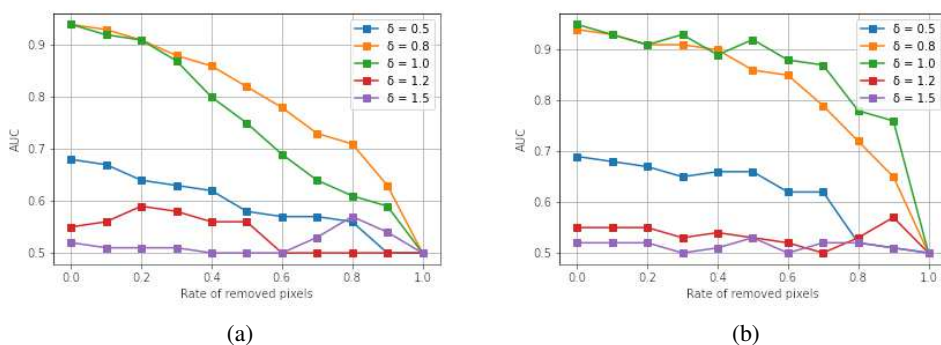


Figure 6: Evaluation of AUC when the ROAR method (a) or the replacing at random strategy is applied (b); on the x-axis the ratio of pixels replaced and on the y-axis the AUC value.

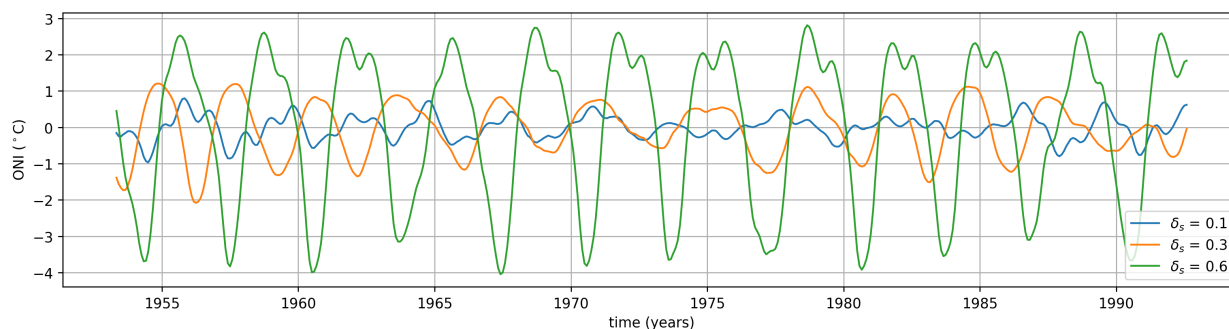


Figure 7: Several time series of ONI calculated from ZC model simulations using  $\delta_s$  parameter values of 0.1, 0.3 and 0.6 using  $\mu = 2.7$ .

(Remove and Retain) introduced in [Mundhenk et al., 2019]. The replacement in the validation sets of an increasingly amount of salient spatial locations with zero-valued pixels rapidly deteriorates the predictive characteristics of the data. It is worthwhile to mention that the CNN does not train any bias term neither in the convolutional layers nor in the dense layers. Thus zero-valued patterns are considered as absolutely non-informative, i.e. the propagation of a zero-valued pattern through the CNN is designed to prevent the activation of any stimulus along the hidden layers. In Fig. 6a we can observe that the removal of the top 50% of the salient pixels via ROAR (actually 24) guarantees a considerable decrease of the AUC. In fact, under the reference case model the AUC scores present a loss equal to 0.20. Contrary to this, when randomly replacing the 50% pixels with zero-valued pixels we can still observe a slighter decrease in the AUC curve under the reference, i.e. a loss equal to 0.03. In addition, similar results can be found when even considering all the distorted physics data analyzed above (Fig. 6b).

### 3.3 Upwelling feedback

We next consider the distortion of the model data due to a wrong representation of the upwelling feedback, represented by the parameter  $\delta_s$  in the ZC model. Figure 7 shows that the ONI's amplitude increases (decreases) for larger (smaller) values of  $\delta_s$ . This behavior is expected because the upwelling feedback is a positive one, enhancing the existing sea surface temperature anomaly further and consequently increasing the amplitude of the ONI. The AUC score versus  $\delta_s$  curve (Fig. 8a) reveals that a particular tuning of the parameter  $\delta_s$  strongly affects the accuracy of the CNN model when trained with distorted data. By construction, the AUC score attains the highest score at the reference value  $\delta_s = 0.3$  (AUC 0.94). For  $\delta_s < 0.3$  the profile of the curve suggests a net degradation in the AUC scores with the lowest score attained at  $\delta_s = 0.15$  (AUC 0.5), whereas at  $\delta_s > 0.3$  the AUC scores remain stable, but still attaining values lower than 0.7. The profile of the UAC has a plateau at values of 0.6 as  $\delta_s$  goes towards the boundary value  $\delta_s = 0.6$ . The evaluation of the loss function (Fig. 8b) as a function of the parameter  $\delta_s$  confirms the results obtained above. At  $\delta_s = 0.3$  the global minimum is achieved, the net degradation occurring at lower and higher  $\delta_s = 0.3$  are still present; the loss function increases monotonically in both cases.

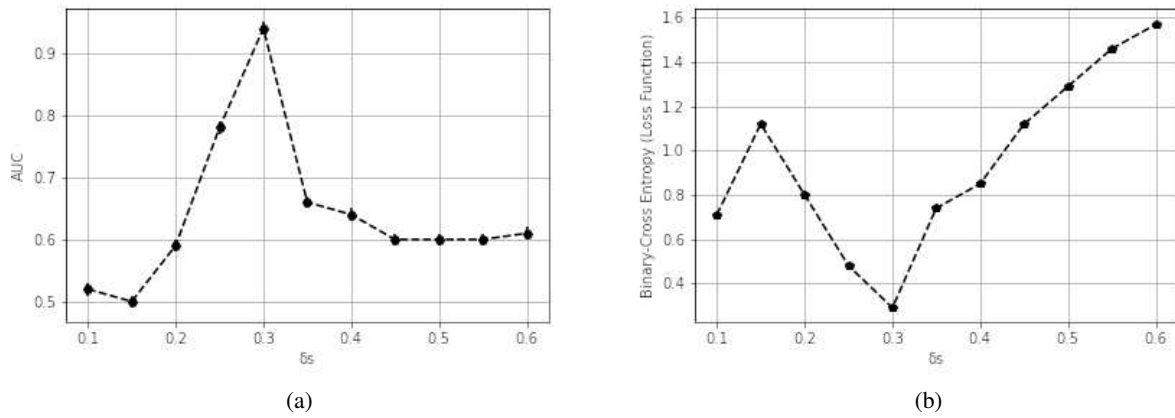


Figure 8: The AUC score (a) and the loss function (b) as a function of the upwelling feedback parameter  $\delta_s$ . Each point represents the mean AUC over 5 different folds; error bars are evaluated via standard error mean.

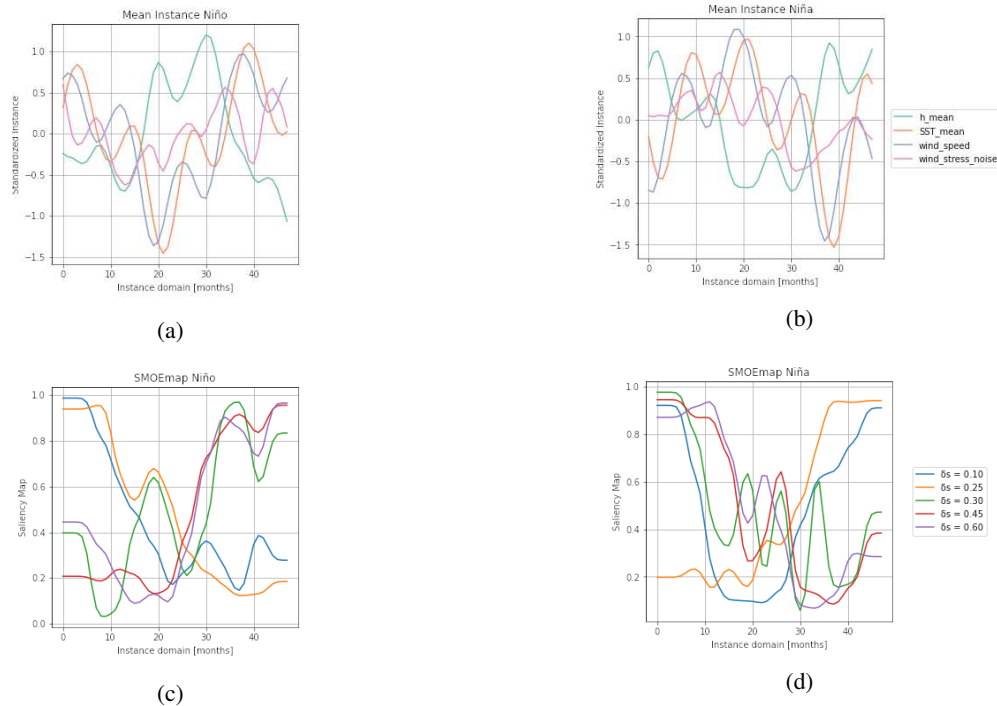


Figure 9: Representation of the mean instance of the test data (reference case; Figs. (a)-(b)) and its saliency maps (Figs. (c)-(d)) for the upwelling distorted case (variation of  $\delta_s$ ). The left column contains the mean instance and the saliency map for the event class El Niño, while on the right column the mean instance and the saliency map for the class La Niña are shown.

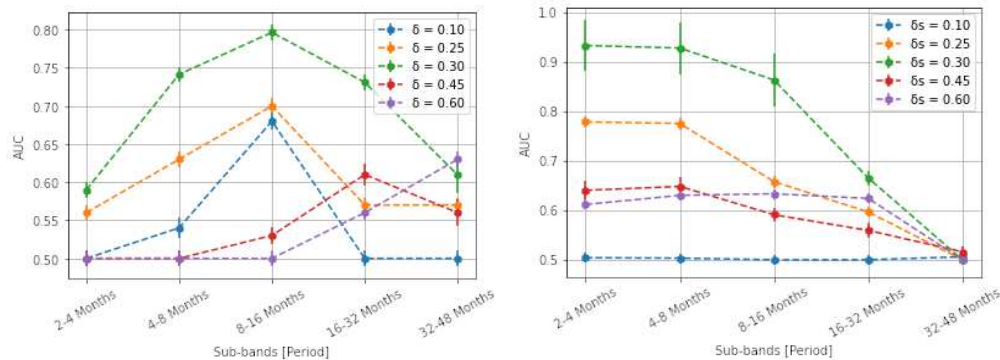


Figure 10: The AUC score for different values of  $\delta_s$  for the event El Niño as a function of a) the band-pass frequency range and b) the cut-off frequency, obtained by filtering the data by a) band-pass Butterworth digital filter and b) a low-pass Butterworth digital filter.

Similarly to the analysis provided for the distortion of the  $\delta$  parameter, we next consider the mean instance (of the reference case data) and its saliency maps. For El Niño events, we can observe that different regions of saliency can be associated to different variation of  $\delta_s$ , i.e. for  $\delta_s < 0.3$  the saliency map indicate the left part of the instance as the most predictive and for  $\delta_s > 0.3$  the right part; for El Niña events the opposite is valid. In particular, cases  $\delta_s = 0.10$  and  $\delta_s = 0.25$  turn out to be very salient around 0-10 month in the saliency map with intensity above 0.8 where a peak occur in both sea surface temperature and wind speed time series. The case  $\delta_s = 0.25$  has actually a larger salient region in the saliency map up to month 20 and includes more interesting patterns, e.g. a more complete sequence of oscillations and a deep trough in the sea surface temperature time-series feature. On the contrary, for cases  $\delta_s = 0.45$  and  $\delta_s = 0.60$  the saliency maps achieve intensities larger than 0.8 around 32-48 months and capture one single broad oscillating peak in the sea surface temperature time-series feature. For La Niña event, we observe that saliency maps of cases  $\delta_s = 0.10$  and  $\delta_s = 0.25$  present intensities higher than 0.8 at 42-48 months. It is interesting to observe that the saliency map of case  $\delta_s = 0.25$  goes above intensity 0.8 and presents a plateau around 32-48 months. Similarly to the El Niño events a deep trough in the sea surface temperature time series feature is captured by the CNN.

The application of band-pass and low-pass filters on the sample instances bring to light a result similar to the analysis done for the parameter  $\delta$ . As we can see in Fig. 10a, the instances for the case  $\delta_s = 0.25$  can partially retrieve the original prediction with AUC 0.70 when a band-pass filter with bandwidth 8-16 months is applied, whereas for the other cases such as  $\delta_s = 0.6$  the original predictions can be retrieved only by oscillations lying within the frequency band corresponding to 32-48 months. The smoothing of the instances via low-pass filter (Fig. 10b) shows that the removal of high-frequency patterns oversimplifies the data; and so the classification task cannot be solved relying on the information contained in the low-frequency data only.

As confirmed by the filtering of the instances, the frequency bands 4-8 months and 8-16 months represent the main frequency bands in the reference case ( $\delta_s = 0.3$ ). Capturing one of these two can retrieve a considerable amount of skill. The case  $\delta_s = 0.25$  focuses a large amount of relevant patters mainly in the frequency band 8-16 months. The filtering with a low-pass digital filters also reveals that a cut-off frequency of 16 months can reduce the AUC in both cases, but a cut-off frequency of 8 months leads to a degradation for the reference case only. In the latter scenario, we register a loss of 0.1 AUC, i.e. a degradation on the same order of magnitude as when testing the reference case data and the data of case  $\delta_s = 0.25$ . Hence, this example shows how a manipulation in the intrinsic characteristic of the instances can lead to a reduction and oversimplification of the instances, i.e. the distortion of the periodicity of data provokes a reduction or missing of some patterns that are fundamental in the classification of the reference case data.

### 3.4 Comparison of CNN and GDNN

To provide a comparison, we also applied the distorted physics approach in the Gaussian Density Neural Network (GDNN) as used in [Petersik and Dijkstra, 2020, ]. The Gaussian density terminology refers to the networks purpose of predicting a Gaussian distribution by producing both a mean and standard deviation as output. The variable to be predicted (or target variable) is also the ONI at a (lead) time in the future. The features used in the GDNN are described by [Petersik and Dijkstra, 2020]: ONI, network graph connectivity metric  $c_2$ , adjusted Hamming distance  $\mathcal{H}^*$  (measure of change in the network graph) and a seasonal cycle (SC) in the form of a cosine. The warm water

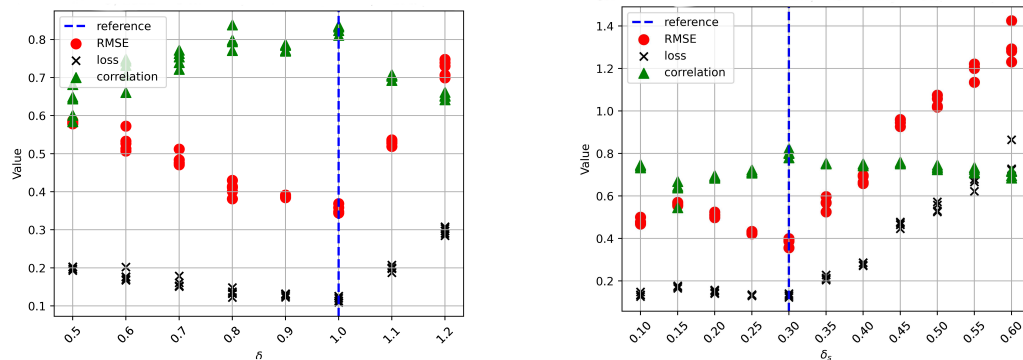


Figure 11: Performance of the GDNN when trained on distorted ZC model data using several values of (a)  $\delta_s$  and (b)  $\delta$ .

volume (WWV, volume of water above the 20 °C thermocline) is not available in the output of ZC model and therefore the thermocline depth itself was used here. All feature datasets are normalized before training.

Training the GDNN consists of a number of ensemble members that are trained in parallel. Each of the members is trained for 100 iterations over 500 epochs with a batch size of 100. The training starts with a random selection of hyper-parameters within bounds defined by the user and is then optimized using the ADAM algorithm [Kingma and Ba, 2014, ] with a user specified learning rate, drop out and Gaussian noise. The resulting ensemble members each predict a mean and standard deviation of the target variable and these predictions are then averaged over the ensemble for the final prediction. Again the lead time is 9 months in the result below.

We use two different measures for the performance of the GDNN: the RMSE and the Pearson correlation; also the loss function is shown. Different simulations give different networks and give different performance values. The GDNN's, when trained on distorted physics data, still perform consistently when varying  $\delta$  or  $\delta_s$ . However, a change in the ONI's amplitude in the training data (such as for higher than reference  $\delta_s$ ) is poorly corrected for, leading to a large overestimation of the predicted variable (e.g. see  $\delta_s = 0.40$  in Fig. 11). The model only tolerates a difference in amplitude between test and training dataset ONI if only a small distortion of the variable is used (e.g.  $\delta_s = 0.35$ ). The ability to compensate for period but not amplitude is explained by the relatively simple architecture of the GDNN. Whereas the former only requires a scalar addition to the input, the latter would require some linear combination of (co)sines to be learned by the neural network.

The attempt of comparing the capability of both CNN and GDNN in detecting El Niño events is made complicated by the intrinsic design of both models. Although both the models are trained to solve the same problem, we have to take into account that the CNN model is a binary classifier, while the GDNN is designed to solve regression problems. In addition, the fact that both models optimize the same loss function does not ensure a relation or a similarity about what the two models learn during the training phase can be found. The two models could focus on capturing totally different features of data, because the outputs of the two models represent two different probabilities, i.e. the CNN estimates the probability of the event itself, whereas the GDNN estimates the probability distribution of the ONI index. However, the ENSO events are based on the behavior of the ONI index and we can exploit this fact to make the outputs of the GDNN more close to those of the CNN. After training the GDNN, we can use the estimation on the Gaussian density to estimate the probability of El Niño events, i.e. the probability that the absolute value of ONI index is greater than 0.5 °C. Thereafter, we can use the AUC metric to compare the performance of the two models.

As we can see in Fig. 12, the GDNN model appears to be less accurate than the CNN model. The reference case data show a lower AUC (compare to Fig. 3a) and we can observe a general reduction of 0.1 AUC respect to the results obtained with the CNN model. When feeding the GDNN model with ZC data with a different tuning of parameters  $\delta$ , we can observe that GDNN tends to be more degraded at  $\delta < 1$  then the CNN model (compare to Fig. 8a); in fact, the AUC can lose up to 0.21 with respect to reference case. Note, that the same tuning of parameter  $\delta$  would reveal a plateau in the AUC score whose values is much closer to that one attained in the reference case. When considering the distortion of parameter  $\delta_s$  we can still appreciate a degradation at values lower than 0.3. However, the decrease in the AUC scores appears milder ( $\sim 0.1$ ) respect to that shown for the CNN model. On the contrary, as  $\delta_s > 0.3$  there is a significant reduction in the AUC scores; with respect to the reference case the AUC scores can now be reduced up to 0.2.

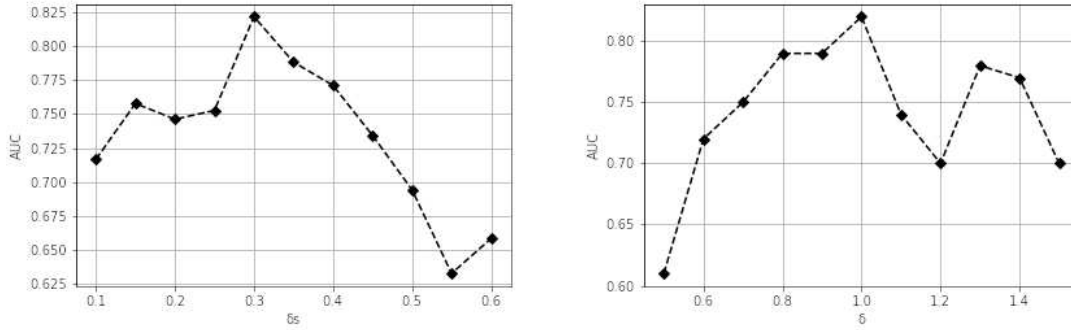


Figure 12: AUC metric for the GDNN when considered as a classifier for both the wave distorted case (a) and the upwelling distorted case (b). On the x-axis the values of ZC parameters ( $\delta$ ,  $\delta_s$ ) and on the y-axis the AUC score.

## 4 Summary and Discussion

This work was strongly motivated to understand the high skill in ENSO prediction obtained with the CNN approach in [Ham et al., 2019a] in particular at long lead times. Although heat maps were presented in [Ham et al., 2019a], their analysis does not connect immediately to the detailed processes of ENSO dynamics, which is also difficult because of the wide range of data they used. In this paper, we introduced distorted physics simulations with the well-known Zebiak-Cane (ZC) model [Zebiak and Cane, 1987, ] to determine how a CNN can perform on real data when trained on data from ‘wrong’ model simulations.

The behavior of the ZC model can be elegantly described by a delay-differential equation [Suarez and Schopf, 1988, Jin, 1997a, ]

$$\frac{dT(t)}{dt} = aT(t) - bT(t-d) - cT^3(t) \quad (2)$$

for the eastern Pacific temperature  $T$  as a function of time  $t$ . Here the constant  $a$  indicates the strength of the positive feedbacks,  $b$  that of the delayed negative feedback (with a delay  $d$  due to equatorial wave dynamics) and  $c$  measures the strength of the nonlinear equilibration.

By distorting the  $\delta$  parameter in the ZC model, we modify the delay  $d$  in (2) and hence mostly the adjustment processes in the equatorial Pacific. When the equatorial wave speeds are distorted, there is an asymmetry in the skill of the CNN. For faster waves  $\delta < 1$ , the performance remains good whereas for  $\delta > 1$  (slower waves) it deteriorates. For example, in case  $\delta = 1.2$  the El Niño event appears to be mainly constituted by slower oscillations, even though the behaviour of the large-scale thermocline depth and sea surface temperature is similar to the reference case. However, the loss of details on shorter time scales leads the model to still reasonably solve the classification task.

By distorting the parameter  $\delta_s$ , we basically modify the feedback parameter  $a$  in (2) and hence the amplitude of the El Niño events. However, also the stability properties of the background climate state are changed as seen through the shift in the Hopf bifurcation with  $\delta_s$  [van der Vaart et al., 2000, ]. For increasing  $\delta_s$  and constant  $\mu$  (as is done here), the background destabilizes as can also be seen in Fig. 7. The case  $\delta_s = 0.1$  (reference case  $\delta_s = 0.3$ ) offers a clear example about how the manipulation in the upwelling feedback can degrade the AUC, i.e. the distortion of the patterns in the data leads to a misplacement and misalignment and reduce the capability of the network in capturing the right patterns at the right (temporal) location. For other cases (e.g.  $\delta_s = 0.25$ ,  $\delta_s = 0.45$  and  $\delta_s = 0.6$ ) the skill of the CNN predictions is reduced less, because the right combination of peaks and valleys in the time series are present. Indeed, the absence of oscillating terms located at frequency band 4-8 months does not allow the CNN to capture all the relevant patterns but only a part of them.

The results indicate that the accuracy of the classification of the El Niño and La Niño events for lead times of 9 months using a CNN approach is strongly related to the capability of the CNN to capture the wave adjustment and feedback processes. The exact combination of specific patterns like peaks and valleys occurring at specific regions of the time domain of all features is essential to generate skill in the CNN predictions. The distorted physics approach can be very useful to look at how a CNN based prediction scheme can represent additional processes then considered here. The work of [Ham et al., 2019a] has already indicated that connections between the Indian-Pacific [Izumo et al., 2010, ] and Atlantic-Pacific [Ham et al., 2013, ] and extratropical-tropical connections [Zhao and Di Lorenzo, 2020, ] are worth investigating. The latter interactions have been described as ocean-atmosphere meridional modes and can in-

fluence ENSO and tropical variability on decadal time scales from both hemispheres independently [Amaya, 2019, ]. However, one cannot do this with the Zebiak-Cane model and needs to do such distorted physics simulations with a more sophisticated global climate model.

## Conflict of Interest

The authors declare to have no conflicts to disclose

## Competing interests

The authors declare to have no competing interest

## Author Contributions

All authors contributed to the design of this study. Results were mainly obtained by GL and IG. The paper was jointly written with contributions from all authors.

## Data Availability Statement

The data that support the findings of this study are openly available in github at [https://github.com/glancia93/Physics-captured-by-data-based-methods-in-El-Nino-prediction\\_PyCODE](https://github.com/glancia93/Physics-captured-by-data-based-methods-in-El-Nino-prediction_PyCODE)

## acknowledgments

The work by HD was sponsored by the Netherlands Science Foundation (NWO) through the project OCENW.M20.277.

## References

- [Adebayo et al., 2018] Adebayo, J., Gilmer, J., Muelly, M., Goodfellow, I., Hardt, M., and Kim, B. (2018). Sanity checks for saliency maps. *arXiv preprint arXiv:1810.03292*.
- [Amaya, 2019] Amaya, D. J. (2019). The Pacific Meridional Mode and ENSO: a Review. *Current Climate Change Reports*, pages 1–13.
- [Arrieta et al., 2020] Arrieta, A. B., Díaz-Rodríguez, N., Del Ser, J., Bennetot, A., Tabik, S., Barbado, A., Garcia, S., Gil-Lopez, S., Molina, D., Benjamins, R., Chatila, R., and Herrera, F. (2020). Explainable Artificial Intelligence (XAI): Concepts, taxonomies, opportunities and challenges toward responsible AI. *Information Fusion*, 58:82–115.
- [Balmaseda et al., 1995] Balmaseda, M. A., Davey, M. K., and Anderson, D. L. T. (1995). Decadal and Seasonal Dependence of ENSO Prediction Skill. *J. Climate*, 8(11):2705–2715.
- [Barnston et al., 2012a] Barnston, A. G., Tippett, M. K., L’Heureux, M. L., Li, S., and DeWitt, D. G. (2012a). Skill of Real-Time Seasonal ENSO Model Predictions during 2002–11: Is Our Capability Increasing? *Bull. Amer. Meteor. Soc.*, 93(5):631–651.
- [Barnston et al., 2012b] Barnston, A. G., Tippett, M. K., L’Heureux, M. L., Li, S., and DeWitt, D. G. (2012b). Skill of Real-Time Seasonal ENSO Model Predictions during 2002–11: Is Our Capability Increasing? *Bull. Amer. Meteor. Soc.*, 93(5):631–651.
- [Butterworth et al., 1930] Butterworth, S. et al. (1930). On the theory of filter amplifiers. *Wireless Engineer*, 7(6):536–541.
- [Chen and Cane, 2008] Chen, D. and Cane, M. A. (2008). El Niño prediction and predictability. *Journal of Computational Physics*, 227(7):3625–3640.
- [Dijkstra, 2005] Dijkstra, H. A. (2005). *Nonlinear Physical Oceanography*, volume 28. Springer.
- [Dijkstra and Neelin, 1995] Dijkstra, H. a. and Neelin, J. (1995). Ocean-atmosphere interaction and the tropical climatology. Part II: Why the Pacific cold tongue is in the east. *Journal of climate*.

- [Dijkstra et al., 2019] Dijkstra, H. A., Petersik, P., Hernández-García, E., and López, C. (2019). The application of machine learning techniques to improve el niño prediction skill. *Frontiers in Physics*, page 153.
- [Duan et al., 2009] Duan, W., Liu, X., Zhu, K., and Mu, M. (2009). Exploring the initial errors that cause a significant "spring predictability barrier" for El Niño events. *Journal of Geophysical Research*, 114(C4).
- [Fedorov et al., 2003] Fedorov, A., Harper, S., Philander, S., Winter, B., and Wittenberg, A. (2003). How predictable is El Niño? *Bulletin of the American Meteorological Society*, 84(7):911–919.
- [Feng and Dijkstra, 2017] Feng, Q. Y. and Dijkstra, H. A. (2017). Climate network stability measures of El Niño variability. *Chaos*, 27(3):035801–15.
- [Gill, 1980] Gill, A. (1980). Some simple solutions for heat-induced tropical circulation. *Quart. J. Roy Meteor. Soc.*, 106:447–462.
- [Goodfellow et al., 2016] Goodfellow, I., Bengio, Y., and Courville, A. (2016). *Deep Learning*. MIT Press. <http://www.deeplearningbook.org>.
- [Ham et al., 2019a] Ham, Y.-G., Kim, J.-H., and Luo, J.-J. (2019a). Deep learning for multi-year ENSO forecasts. *Nature Publishing Group*, pages 1–17.
- [Ham et al., 2019b] Ham, Y.-G., Kim, J.-H., and Luo, J.-J. (2019b). Deep learning for multi-year enso forecasts. *Nature*, 573(7775):568–572.
- [Ham et al., 2013] Ham, Y.-G., Kug, J.-S., Park, J.-Y., and Jin, F.-F. (2013). Sea surface temperature in the north tropical Atlantic as a trigger for El Niño/Southern Oscillation events. *Nature Geosci*, 6(2):112–116.
- [Hamming, 1998] Hamming, R. W. (1998). *Digital filters*. Courier Corporation.
- [Hou et al., 2019] Hou, M., Duan, W., and Zhi, X. (2019). Season-dependent predictability barrier for two types of El Niño revealed by an approach to data analysis for predictability. *Climate Dynamics*, 53(9):5561–5581.
- [Izumo et al., 2010] Izumo, T., Vialard, J., Lengaigne, M., de Boyer Montegut, C., Behera, S. K., Luo, J.-J., Cravatte, S., Masson, S., and Yamagata, T. (2010). Influence of the state of the Indian Ocean Dipole on the following year's El Niño. *Nature Geosci*, 3(3):168–172.
- [Jin, 1997a] Jin, F.-F. (1997a). An equatorial recharge paradigm for ENSO. I: Conceptual Model. *J. Atmos. Sci.*, 54:811–829.
- [Jin, 1997b] Jin, F.-F. (1997b). An equatorial recharge paradigm for ENSO. II: A stripped-down coupled model. *J. Atmos. Sci.*, 54:830–8847.
- [Jin et al., 1994] Jin, F.-F., Neelin, J., and Ghil, M. (1994). El Niño on the devil's staircase: Annual subharmonic steps to chaos. *Science*, 264:70–72.
- [Kingma and Ba, 2014] Kingma, D. P. and Ba, J. (2014). Adam: A Method for Stochastic Optimization. *arXiv:1412.6980 [cs]*. arXiv: 1412.6980.
- [Lakshminarayanan et al., 2017] Lakshminarayanan, B., Pritzel, A., and Blundell, C. (2017). Simple and scalable predictive uncertainty estimation using deep ensembles. In Guyon, I., Luxburg, U. V., Bengio, S., Wallach, H., Fergus, R., Vishwanathan, S., and Garnett, R., editors, *Advances in Neural Information Processing Systems 30*, pages 6402–6413. Curran Associates, Inc.
- [Latif et al., 1998] Latif, M., Anderson, D., Barnett, T., Cane, M., Kleeman, R., Leetmaa, A., O'Brien, J. J., Rosati, A., and Schneider, E. (1998). A review of the predictability and prediction of ENSO. *Journal of Geophysical Research*.
- [Latif and Barnett, 1994] Latif, M. and Barnett, T. P. (1994). Causes of decadal climate variability over the North Pacific and North America. *Science*, 266:634–637.
- [L'Heureux et al., 2017] L'Heureux, M. L., Takahashi, K., Watkins, A. B., Barnston, A. G., Becker, E. J., Di Liberto, T. E., Gamble, F., Gottschalck, J., Halpert, M. S., Huang, B., Mosquera-Vásquez, K., and Wittenberg, A. T. (2017). Observing and Predicting the 2015/16 El Niño. *Bull. Amer. Meteor. Soc.*, 98(7):1363–1382.
- [Lian et al., 2014] Lian, T., Chen, D., Tang, Y., and Wu, Q. (2014). Effects of westerly wind bursts on El Niño: A new perspective. *Geophys. Res. Lett.*, 41(10):3522–3527.
- [McPhaden, 2003] McPhaden, M. J. (2003). Tropical Pacific Ocean heat content variations and ENSO persistence barriers. *Geophysical Research Letters*, 30(9):2705–2709.
- [McPhaden et al., 2015] McPhaden, M. J., Timmermann, A., Widlansky, M. J., Balmaseda, M. A., and Stockdale, T. N. (2015). The curious case of the El Niño that never happened: A perspective from 40 years of progress in climate research and forecasting. *Bull. Amer. Meteor. Soc.*, 96(10):1647–1665.

- [Montavon et al., 2019] Montavon, G., Binder, A., Lapuschkin, S., Samek, W., and Müller, K.-R. (2019). Layer-wise relevance propagation: an overview. *Explainable AI: interpreting, explaining and visualizing deep learning*, pages 193–209.
- [Mu et al., 2007] Mu, M., Sun, L., and Dijkstra, H. a. (2007). The sensitivity and stability of the ocean’s thermohaline circulation to finite amplitude perturbations. *arXiv preprint physics/0702083*, pages 1–40.
- [Mundhenk et al., 2019] Mundhenk, T. N., Chen, B. Y., and Friedland, G. (2019). Efficient saliency maps for explainable ai. *arXiv preprint arXiv:1911.11293*.
- [Neelin, 1991] Neelin, J. D. (1991). The slow sea surface temperature mode and the fast-wave limit- Analytic theory for tropical interannual oscillations and experiments in a hybrid coupled model. *Journal of the atmospheric sciences*.
- [Neelin et al., 1998] Neelin, J. D., Battisti, D. S., Hirst, A. C., Jin, F.-F., Wakata, Y., Yamagata, T., and Zebiak, S. (1998). ENSO theory. *Journal of Geophysical Research*, 103(C7):14261–14290.
- [Petersik and Dijkstra, 2020] Petersik, P. J. and Dijkstra, H. A. (2020). Probabilistic forecasting of el niño using neural network models. *Geophysical Research Letters*, 47(6):e2019GL086423.
- [Preisendorfer, 1988] Preisendorfer, R. W. (1988). *Principal Component Analysis in Meteorology and Oceanography*. Elsevier, Amsterdam, The Netherlands.
- [Saha et al., 2014] Saha, S., Moorthi, S., Wu, X., Wang, J., Nadiga, S., Tripp, P., Behringer, D., Hou, Y.-T., Chuang, H.-y., Iredell, M., et al. (2014). The NCEP climate forecast system version 2. *Journal of Climate*, 27(6):2185–2208.
- [Selvaraju et al., 2017] Selvaraju, R. R., Cogswell, M., Das, A., Vedantam, R., Parikh, D., and Batra, D. (2017). Grad-cam: Visual explanations from deep networks via gradient-based localization. In *Proceedings of the IEEE international conference on computer vision*, pages 618–626.
- [Srivastava et al., 2014] Srivastava, N., Hinton, G., Krizhevsky, A., Sutskever, I., and Salakhutdinov, R. (2014). Dropout: a simple way to prevent neural networks from overfitting. *The Journal of Machine Learning Research*, 15(1):1929–1958.
- [Suarez and Schopf, 1988] Suarez, M. and Schopf, P. S. (1988). A delayed action oscillator for ENSO. *J. Atmos. Sci.*, 45:3283–3287.
- [Tang et al., 2018] Tang, Y., Zhang, R.-H., Liu, T., Duan, W., Yang, D., Zheng, F., Ren, H., Lian, T., Gao, C., Chen, D., and Mu, M. (2018). Progress in ENSO prediction and predictability study. *National Science Review*, 5(6):826–839.
- [Tian and Duan, 2015] Tian, B. and Duan, W. (2015). Comparison of the initial errors most likely to cause a spring predictability barrier for two types of El Niño events. *Climate Dynamics*, 47(3):779–792.
- [Timmermann et al., 2018] Timmermann, A., An, S.-I., Kug, J.-S., Jin, F.-F., Cai, W., Capotondi, A., Cobb, K., Lengaigne, M., McPhaden, M. J., Stuecker, M. F., Stein, K., Wittenberg, A. T., Yun, K.-S., Bayr, T., Chen, H.-C., Chikamoto, Y., Dewitte, B., Dommenges, D., Grothe, P., Guilyardi, E., Ham, Y.-G., Hayashi, M., Ineson, S., Kang, D., Kim, S., Kim, W., Lee, J.-Y., Li, T., Luo, J.-J., McGregor, S., Planton, Y., Power, S., Rashid, H., Ren, H.-L., Santoso, A., Takahashi, K., Todd, A., Wang, G., Wang, G., Xie, R., Yang, W.-H., Yeh, S.-W., Yoon, J., Zeller, E., and Zhang, X. (2018). El Niño–Southern Oscillation complexity. *Nature*, pages 1–11.
- [Tziperman et al., 1994] Tziperman, E., Toggweiler, J. R., Bryan, K., and Feliks, Y. (1994). Instability of the thermohaline circulation with respect to mixed boundary conditions: Is it really a problem for realistic models? *Journal of Physical Oceanography*, 24(2):217–232.
- [van der Vaart et al., 2000] van der Vaart, P. C. F., Dijkstra, H. a., and Jin, F. F. (2000). The Pacific Cold Tongue and the ENSO Mode: A Unified Theory within the Zebiak–Cane Model. *Journal of the Atmospheric Sciences*, 57(7):967–988.
- [Yan et al., 2020] Yan, J., Mu, L., Wang, L., Ranjan, R., and Zomaya, A. Y. (2020). Temporal convolutional networks for the advance prediction of enso. *Scientific reports*, 10(1):1–15.
- [Yu et al., 2012] Yu, Y., Mu, M., and Duan, W. (2012). Does model parameter error cause a significant spring predictability barrier for El Niño events in the Zebiak-Cane model? *J. Climate*, 25:1263–1277.
- [Zebiak and Cane, 1987] Zebiak, S. E. and Cane, M. A. (1987). A model El Niño–Southern Oscillation. *Monthly Weather Review*, 115:2262–2278.
- [Zhang et al., 2019] Zhang, Z., Ren, B., and Zheng, J. (2019). A unified complex index to characterize two types of ENSO simultaneously. *Scientific Reports*, pages 1–8.
- [Zhao and Di Lorenzo, 2020] Zhao, Y. and Di Lorenzo, E. (2020). The impacts of Extra-tropical ENSO Precursors on Tropical Pacific Decadal-scale Variability. *Scientific Reports*, pages 1–12.



[Zhou et al., 2016] Zhou, B., Khosla, A., Lapedriza, A., Oliva, A., and Torralba, A. (2016). Learning deep features for discriminative localization. In *Proceedings of the IEEE conference on computer vision and pattern recognition*, pages 2921–2929.